Electronic Supplementary Material (ESI) for Journal of Materials Chemistry A.

Supporting Information

Incorporation of Fe^{3+} into MnO_2 birnessite towards improved energy storage: Impact on the structure and the charge storage mechanisms

Ronan Invernizzi,[a] Vadim M. Kovrugin,[a] Louise Molinié,[a] Antonella Iadecola,[b] Mathieu Duttine,[a] Lydie Bourgeois,[c] Jacob Olchowka,[a,b,d*] Liliane Guerlou-Demourgues,[a,b,d*]

[a] Univ. Bordeaux, CNRS, Bordeaux INP, ICMCB, UMR 5026, F-33600 Pessac, France

[b] RS2E, Réseau Français sur le Stockage Electrochimique de l'Energie, CNRS FR 3459, 80039 Amiens Cedex 1, France

[c] Univ. Bordeaux, CNRS, Bordeaux INP, ISM, UMR 5255, F-33400 Talence, France

[d] ALISTORE-ERI European Research Institute, CNRS FR 3104, 80039 Amiens Cedex 1, France

Corresponding Authors

* jacob.olchowka@icmcb.cnrs.fr
* liliane.guerlou-demourgues@enscbp.fr

Part S1: Birnessite polytypes:

In total, there are 7 principally different periodic slab stacking modes in birnessite with either prismatic or octahedral interlayer environments for alkali metal cations depending on the shift of successive slabs relative to each other. Among them, it is possible to distinguish one simplest polytype with 1 layer per cell, two polytypes with 2 layers per cell, and four 3-layers polytypes[1] (see ref. for more details).

Moreover, the birnessite-type structures are described with either expected hexagonal (vacancy-bearing) or pseudo-hexagonal orthogonal (vacancy-free) symmetry of MnO_2 slabs. The latter results from the presence of a relatively higher amount of Mn^{3+} cations in the slabs leading to a distortion of transition metal octahedra due to the Jahn-Teller effect[2]. Hence, each of 7 polytypes can exist in both, hexagonal or orthogonal systems, which implies a doubling of the number of possible birnessite structures.

Given an ideal classic brucite-like slab made up of edge-shared MnO_2 octahedra, its structure naturally aligns with hexagonal 'honeycomb' symmetry. However, with the introduction of Mn^{3+} cations, distortions in the manganese octahedra and vacancies may arise. As a consequence, while the MnO_2 slab might still appear hexagonal to the eye, its precise symmetry decreases, causing the layer to adopt an orthogonal symmetry. Hence, the term "pseudo-hexagonal" symmetry is used to describe its real orthogonal symmetry – but it's used in a purely visual descriptive sense. Refer to the figure below for clarity.

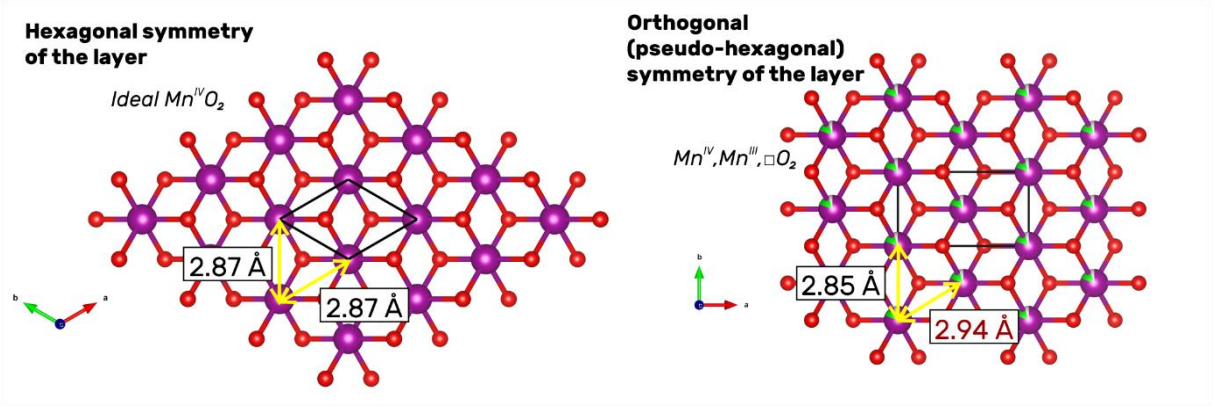

When analyzing the full symmetry of the birnessite structure, which includes both the symmetry of the slabs and the interlayer, various descriptions from literature point to different possible space groups: hexagonal (e.g., P63/mmc), orthorhombic (e.g., Ccmm), monoclinic (e.g., C2/m), and triclinic (e.g., P-1) space groups.

Finally, the description of these structures is rather complicated and confusing in the literature since there are two nomenclatures used for a classification of the polytypes so far: the traditional mineralogical Ramsdell system[3] used by Drits *et al* [1] based on the symmetry of the MnO_2 slabs, and the alternative

notation based on the interlayer type usually used by material scientists originally introduced by Delmas *et al.* [4].

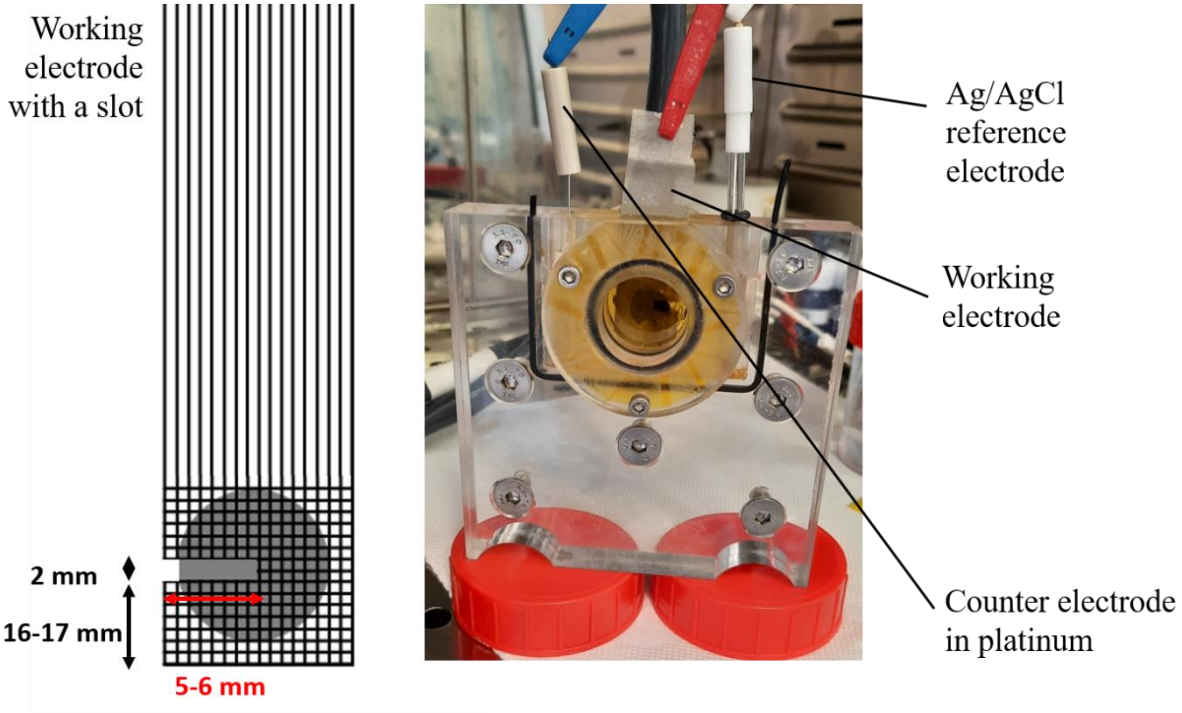

Figure S1: Operando cell from IMN (Nantes) used for operando XAS at ROCK beamline.

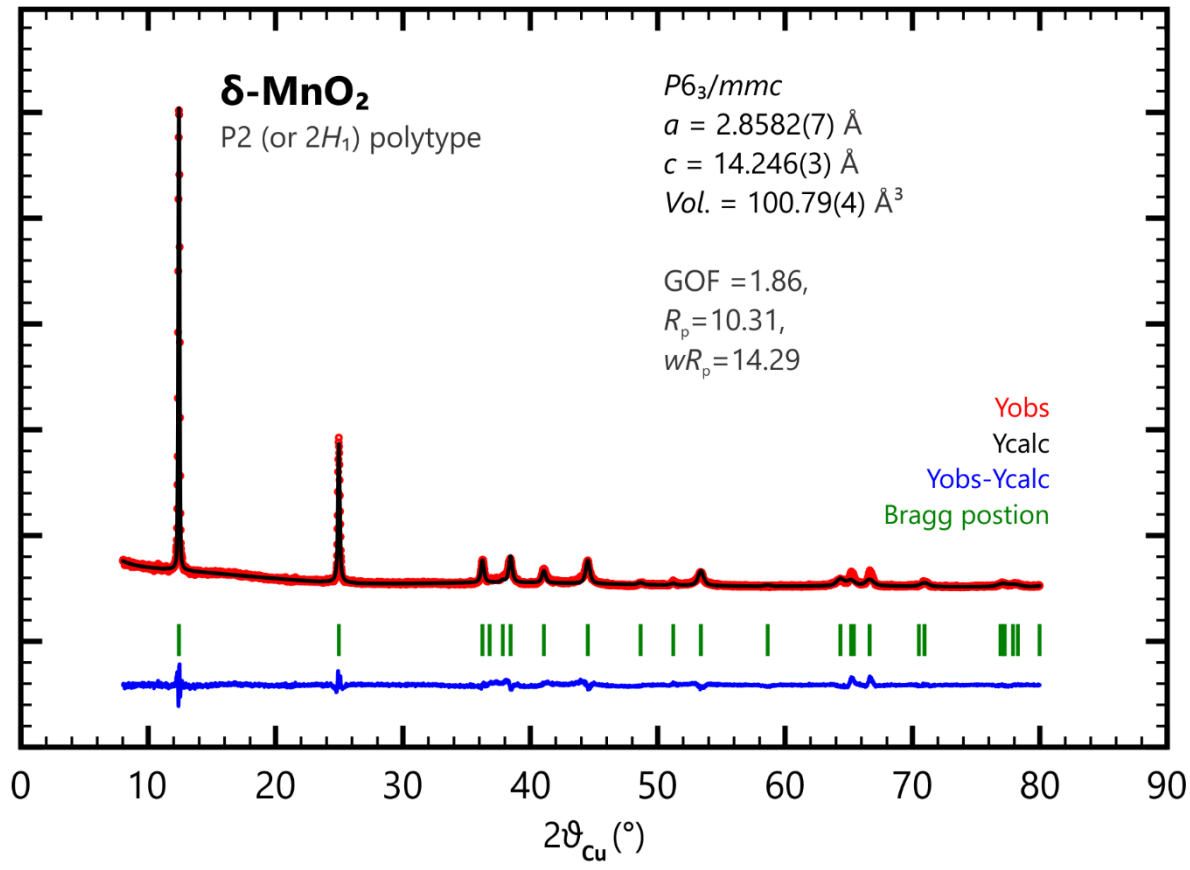

Figure S2: Results of the Rietveld refinement of the crystal structure of δ-MnO_2. Mineralogical polytype notation is given brackets.

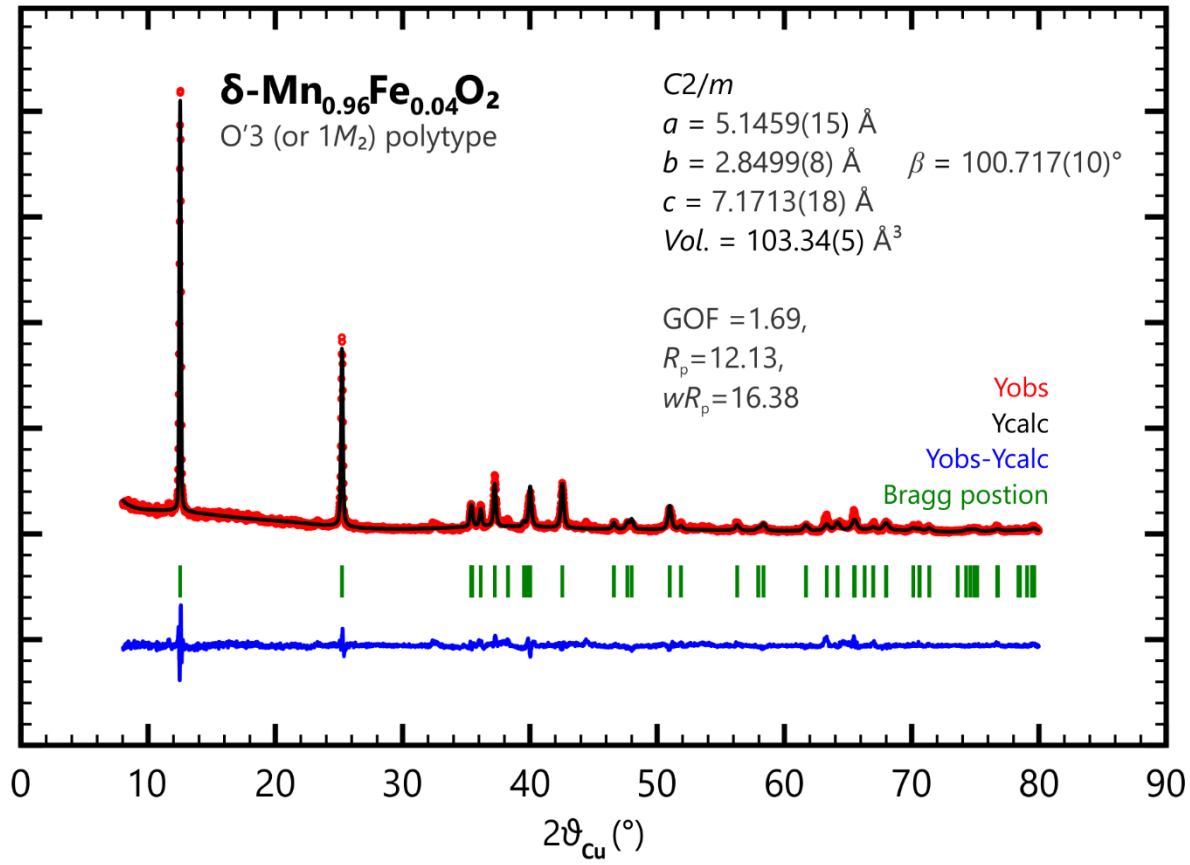

Figure S3: Results of the Rietveld refinement of the crystal structure of δ-$Mn_{0.96}Fe_{0.04}O_2$. Mineralogical polytype notation is given brackets.

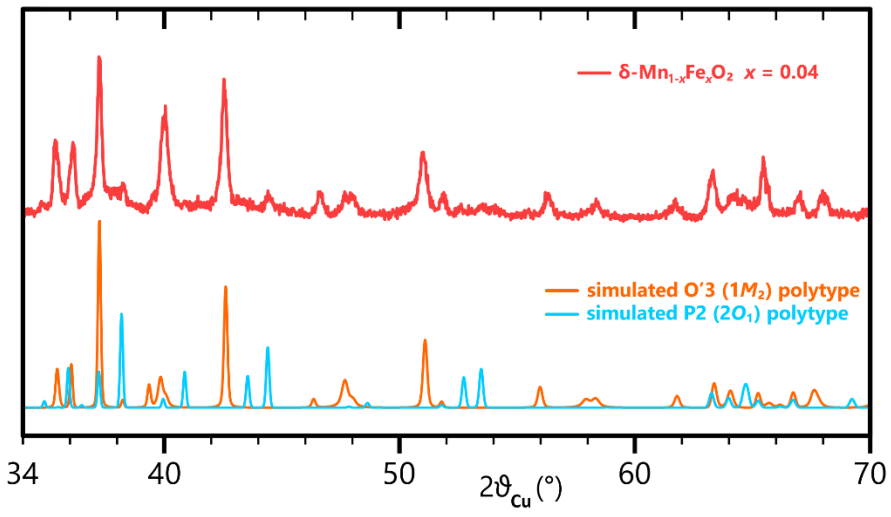

Figure S4: (Top) Powder XRD patterns of δ-$Mn_{1-x}Fe_xO_2$, x = 0.04 (red). (Bottom) Simulated XRD patterns corresponding to idealized birnessite polytypes O'3 (orange) and P2 (light blue).

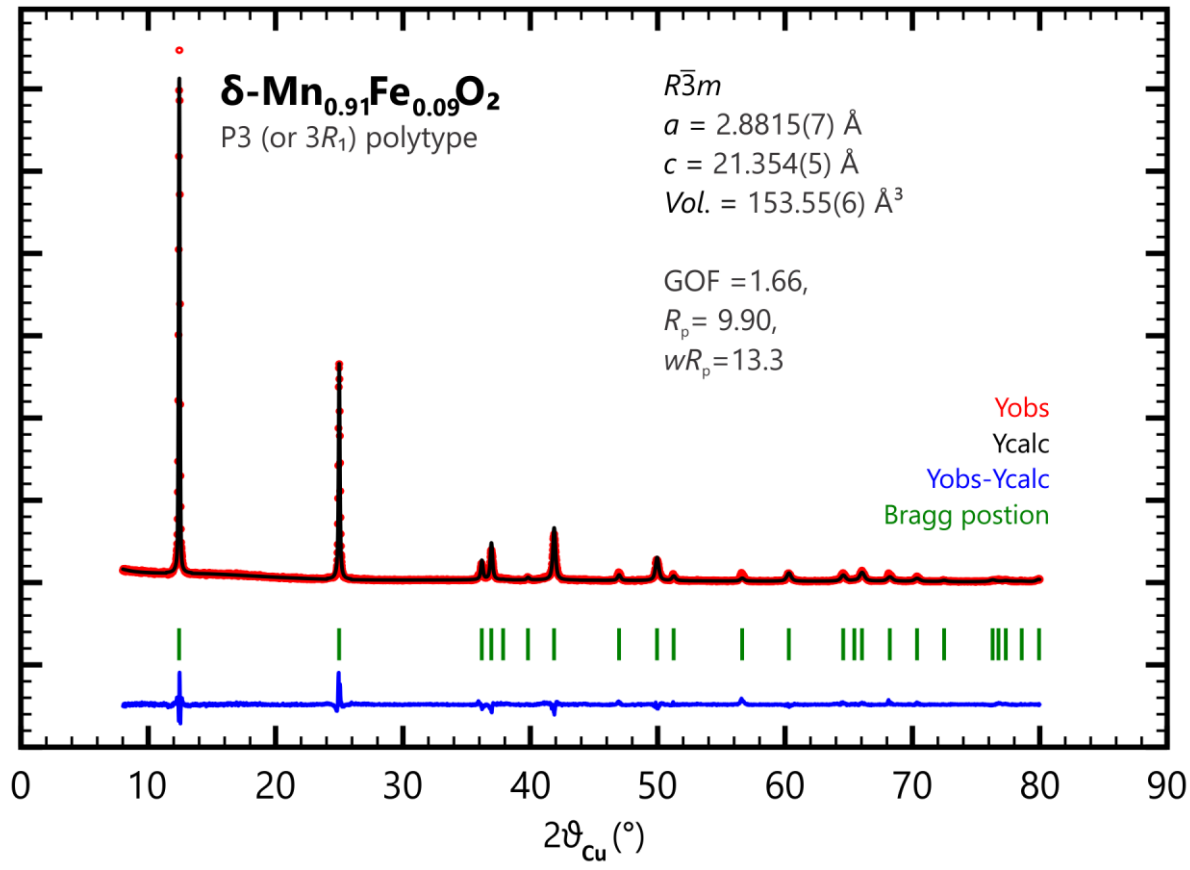

Figure S5: Results of the Rietveld refinement of the crystal structure of δ-$Mn_{0.91}Fe_{0.09}O_2$. Mineralogical polytype notation is given brackets.

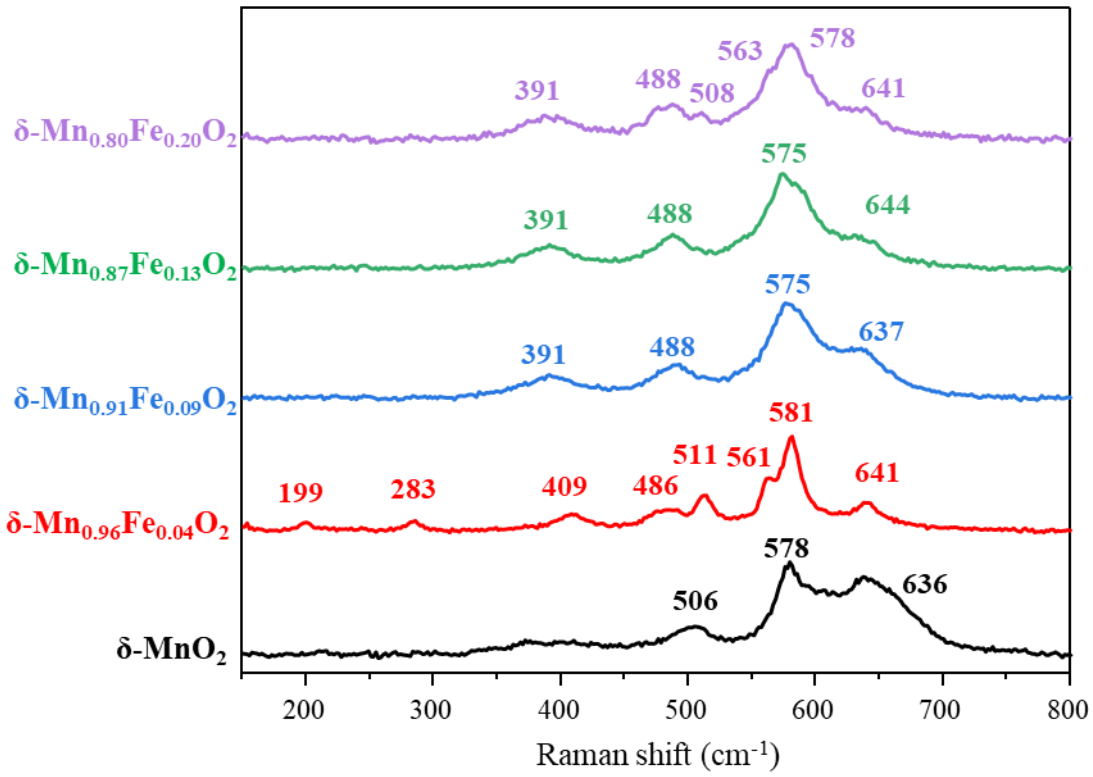

Figure S6: Raman spectra of the series of iron-birnessites δ-MnO_2 (black curve), δ-$Mn_{0.96}Fe_{0.04}O_2$ (red curve), δ-$Mn_{0.91}Fe_{0.09}O_2$ (blue curve), δ-$Mn_{0.87}Fe_{0.13}O_2$ (green curve) and δ-$Mn_{0.80}Fe_{0.20}O_2$ (purple curve).

Raman scattering measurements were performed with a Horiba Jobin Yvon Labram HR-800 micro-spectrometer, using a 514.5 nm excitation wavelength and a power adjusted to ca. 50 µW.

Raman spectra confirm the change of symmetry depending on the iron content within the birnessite-type phase.

The spectrum of δ-MnO_2 (black curve) displays three bands at 506, 578 and 636 cm^{-1} that are typical for a birnessite with a hexagonal symmetry and can be attributed to the stretching and bending of [MnO_6]. The overlapping of several bands between 550 cm^{-1} and 700 cm^{-1} leading to a broad signal is most probably induced by the presence of interlayer Mn^{3+} and thus, different Mn environments.

The symmetry lowering for δ-$Mn_{0.96}Fe_{0.04}O_2$ (red curve) can clearly be observed with the apparition of several new bands and perfectly correlates the structural refinement in the monoclinic system.

Finally, the spectra of δ-$Mn_{0.91}Fe_{0.09}O_2$ (blue curve), δ-$Mn_{0.87}Fe_{0.13}O_2$ (green curve) and δ-$Mn_{0.80}Fe_{0.20}O_2$ (purple curve) are similar and display the main peaks at 488 cm^{-1}, 575 cm^{-1} and ca.640 cm^{-1} that correspond to the stretching and bending vibration modes of [MnO_6], in perfect agreement with a hexagonal birnessite reported by Osaka et al.[5]. Besides, the additional peaks observed for δ-$Mn_{0.80}Fe_{0.20}O_2$ (i.e at 508 cm^{-1}) fits with the presence of an additional O'3 phase observed by diffraction.

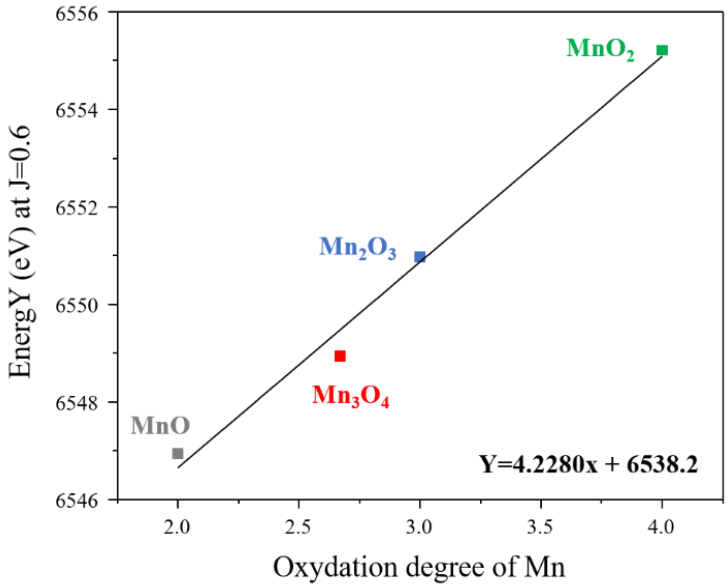

Figure S7: Dependence between the oxidation degree of manganese for the reference materials (MnO, Mn_3O_4, Mn_2O_3 and MnO_2) and the threshold energy value at J=0.7 (Y= 4.2368 X + 6539.2). An energy of 6554.50 eV is found for δ-$Mn_{0.96}Fe_{0.04}O_2$ and 6554.75 eV for all the P-type birnessites, leading to average Mn oxidation state of 3.61 and 3.67 respectively.

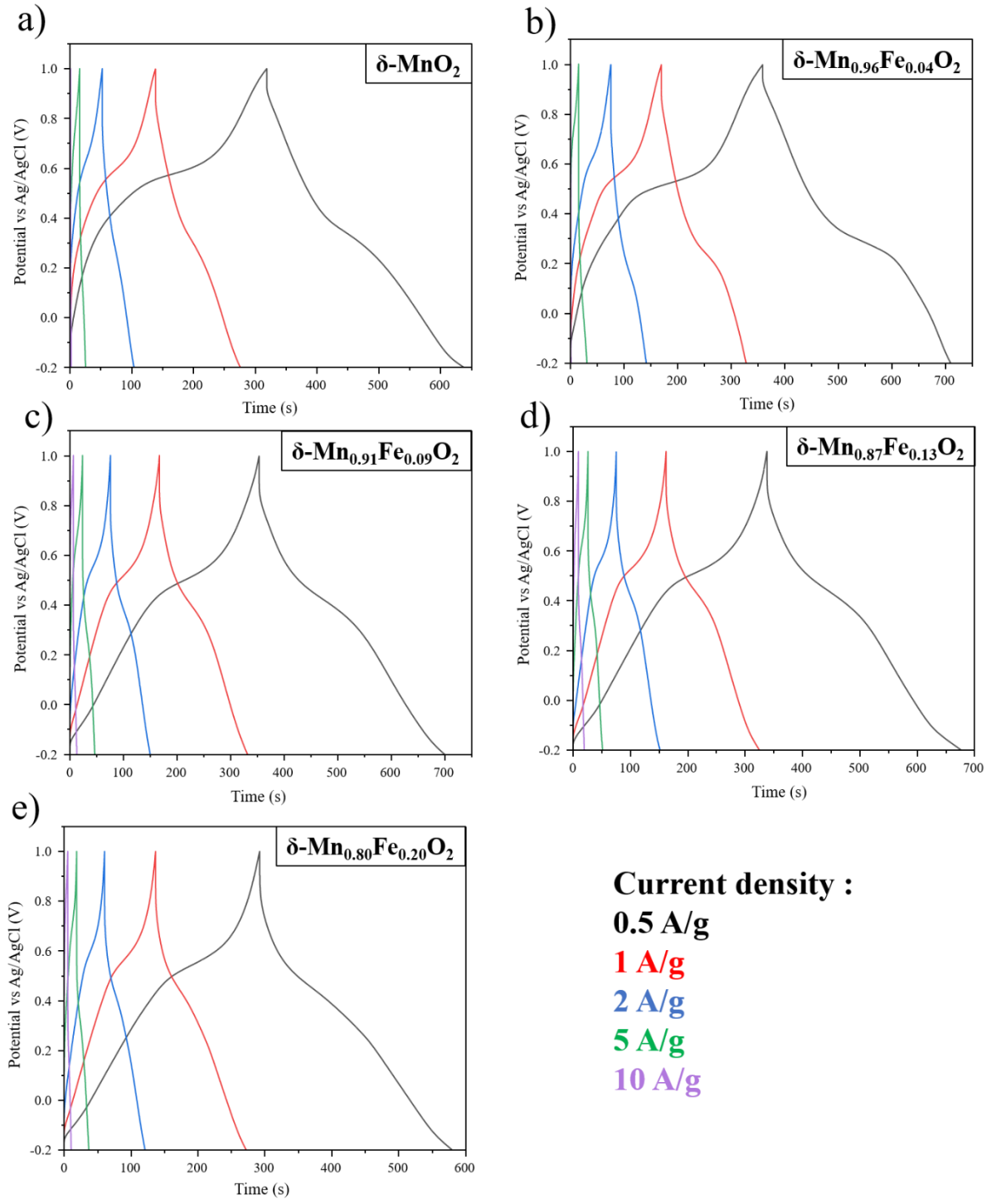

Figure S8: Galvanostatic charge-discharge curves from 0.5 A/g to 10 A/g in 0.5M K_2SO_4. When the current density increases to 10 A/g, the profile becomes a line which demonstrates the limited alkaline diffusion involved in the energy storage reactions.

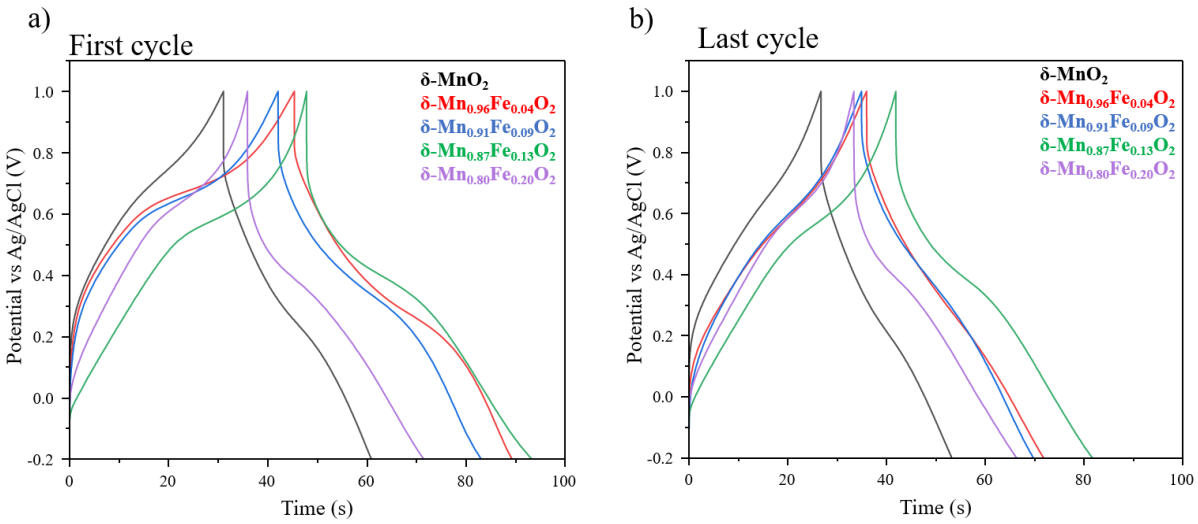

Figure S9: Galvanostatic charge-discharge in 0.5M K_2SO_4 at 3 A/g of the series of samples. The graph a) reports the first cycle while the graph b) the 5000th cycle.

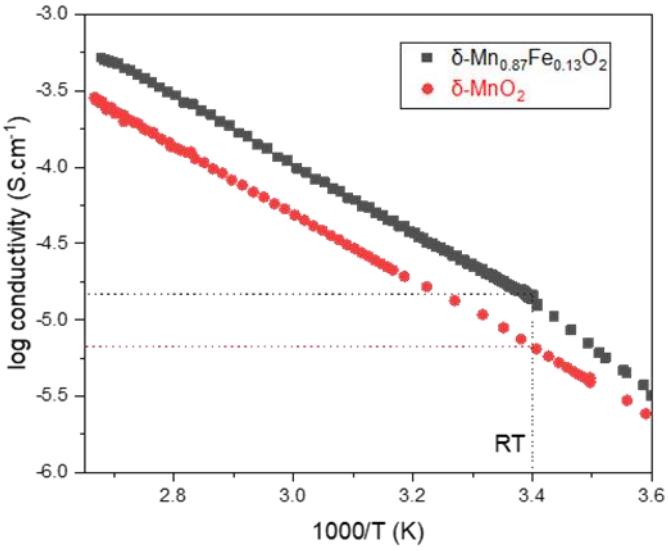

Figure S10: Comparison of the electrical conductivity versus temperature using the 4-point probe Method. The measurements were performed on pellets that were prepared by pressing the birnessite polycrystalline sample at 5 tons.

To compare the conductivity between δ-MnO_2 and δ-$Mn_{1-x}FexO_2$ we performed 4-probe measurements. The figure above compares the conductivity versus temperature of δ-MnO_2 and δ-$Mn_{0.87}Fe_{0.13}O_2$. The data show that the RT electrical conductivity is improved in the presence of Fe in the metal oxide layer.

Table S1: Chemical compositions of the different materials, determined by combining ICP-OES, CHNS, Mössbauer and XAS. The values obtained from the Rietveld refinement of the structural data are italicized in the respective cells below.

Sample	% K (mass.)	% Fe (mass.)	% Mn (mass.)	Atomic ratio K/(Mn+Fe) *[from str.]*	Oxydation degree of Mn	Chemical formula
δ-MnO_2	10.1	/	45.1	0.30 *[0.32]*	3.67	$H_{0.03}{}^{+}K_{0.30}{}^{+}(H_2O)_{0.32}Mn^{3.67+}O_2$ / *$[K_{0.300}\ Mn^{3+}{}_{0.063}\ (H_2O)_{0.74}]\{Mn^{4+}{}_{0.878}\ \square_{0.122}\ O_2\}$*
δ-$Mn_{0.96}Fe_{0.04}O_2$	10.4	1.8	42.9	0.34 *[0.32]*	3.61	$H_{0.07}{}^{+}K_{0.34}{}^{+}(H_2O)_{0.28}[Fe_{0.04}{}^{3+}Mn_{0.96}{}^{3.61+}O_2]$ / *$[K_{0.324}\ (H_2O)_{1.05}]\ \{Fe^{3+}{}_{0.039}\ (Mn^{3+}{}_{0.285}, Mn^{4+}{}_{0.676})_{\Sigma=0.961}\ O_2\}$*
δ-$Mn_{0.91}Fe_{0.09}O_2$	7.3	4.4	43.7	0.23 *[0.21]*	3.67	$H_{0.16}{}^{+}K_{0.23}{}^{+}(H_2O)_{0.32}[Fe_{0.09}{}^{3+}Mn_{0.91}{}^{3.67+}O_2]$ / *$[K_{0.213}\ (H_2O)_{1.04}]\ \{Fe^{3+}{}_{0.09}\ (Mn^{3+}{}_{0.123}, Mn^{4+}{}_{0.787})_{\Sigma=0.91}\ O_2\}$*
δ-$Mn_{0.87}Fe_{0.13}O_2$	7.4	6.4	42.3	0.22	3.67	$H_{0.20}{}^{+}K_{0.22}{}^{+}(H_2O)_{0.26}[Fe_{0.13}{}^{3+}Mn_{0.87}{}^{3.67+}O_2]$
δ-$Mn_{0.80}Fe_{0.20}O_2$	9.2	8.5	35.4	0.29	3.67	$H_{0.17}{}^{+}K_{0.29}{}^{+}(H_2O)_{0.24}[Fe_{0.20}{}^{3+}Mn_{0.80}{}^{3.67+}O_2]$

Based on the results of ICP-OES and CHNS analyses and the oxidation degree of the transition metal determined by ^{57}Fe Mössbauer and X-ray adsorption spectroscopy (see below), the synthesized materials can be described by precise chemical formulae listed in Table S1, which are in general agreement with the structural formulae resulting from the Rietveld refinement.

Table S2: Fractional atomic coordinates and equivalent isotropic displacement parameters for $K_{0.300}\,Mn^{III}_{0.063}(Mn^{IV}_{0.878}\,\square_{0.122}O_2)\cdot 0.74(H_2O)$ *(or* δ*-*MnO_2*).*

Atome	Wycoff site	*x*	*y*	*z*	U_{iso}*/U_{eq}	Occ. (<1)
Mn1	2a	0	0	0	0.004 (3)*	0.878
O1	4f	0.666667	0.333333	0.0513 (5)	0.0274*	
K1	6h	0.222 (7)	0.778 (7)	0.25	0.0991*	0.0999
Mn2	4e	0	0	0.160(4)	0.21 (19)*	0.0315
O2	2c	0.333333	0.666667	0.25	0.0835*	0.245 (18)
O3	6h	0.175 (15)	0.088 (8)	0.25	0.047*	0.1652

Table S3: Fractional atomic coordinates and equivalent isotropic displacement parameters for $K_{0.324}(Fe^{III}_{0.039}Mn^{III,IV}_{0.961}O_2)\cdot 1.05(H_2O)$ *(or* δ-$Mn_{0.96}Fe_{0.04}O_2$*).*

Atome	Wyck.	*x*	*y*	*z*	U_{iso}*/U_{eq}	Occ. (<1)
Mn1	2a	0.0864*	0	0	0.045 (8)*	0.961
Fe1	2a	0	0	0	0.045 (8)*	0.039
O1	4i	0.3634 (16)	0	0.1293 (12)	0.046 (8)*	
O3	2c	0	0	0.5	0.0982*	0.27 (3)
K1	4i	−0.269497	0	0.505106	0.0864*	0.162
O2	4i	−0.264 (7)	0	0.514 (4)	0.0864*	0.392 (17)

Table S4: Fractional atomic coordinates and equivalent isotropic displacement parameters for $K_{0.213}(Fe^{III}_{0.09}Mn^{III,IV}_{0.91}O_2)\cdot 1.04(H_2O)$ *(or* δ-$Mn_{0.91}Fe_{0.09}O_2$*).*

Atome	**Wyckoff site**	*x*	*y*	*z*	U_{iso}*/U_{eq}	Occ. (<1)
Mn1	3a	0	0	0	0.2 (5)*	0.91
Fe1	3a	0	0	0	0.2 (5)*	0.09
O1	6c	0.666667	0.333333	−0.0398 (2)	0.1 (5)*	
O2	18h	0.296 (3)	0.1480 (14)	−0.16513	0.0 (5)*	0.173 (2)
K1	18h	0.13 (2)	0.066 (10)	−0.16513	0.0 (5)*	0.0355

References:

(1) Drits, V. A.; Lanson, B.; Gaillot, A.-C. Birnessite Polytype Systematics and Identification by Powder X-Ray Diffraction. *Am. Mineral.* 2007, **92** (5–6), 771–788. https://doi.org/10.2138/am.2007.2207.

(2) Drits, V. A.; Silvester, E.; Gorshkov, A. I.; Manceau, A. Structure of Synthetic Monoclinic Na-Rich Birnessite and Hexagonal Birnessite: I. Results from X-Ray Diffraction and Selected-Area Electron Diffraction. *Am. Mineral* 1997, **82** (9–10), 946–961.

(3) Ramsdell, L. S. Studies on Silicon Carbide. *Am. Mineral.* 1947, **32** (1–2), 64–82.

(4) Delmas, C.; Fouassier, C.; Hagenmuller, P. Structural Classification and Properties of the Layered Oxides. *Physica B+C* 1980, **99** (1–4), 81–85. https://doi.org/10.1016/0378-4363(80)90214-4.

(5) Ogata, A.; Komaba, S.; Baddour-Hadjean, R. Doping Effects on Structure and Electrode Performance of K-Birnessite-Type Manganese Dioxides for Rechargeable Lithium Battery. *Electrochimica Acta* 2008, **53**, 3084-3093. https://doi.org/10.1016/j.electacta.2007.11.038